Wetting Resistance at Its Topographical Limit: The Benefit of Mushroom and Serif T Structures

René Hensel,[†,‡,#] Ralf Helbig,[†,#] Sebastian Aland,[§] Hans-Georg Braun,[†] Axel Voigt,[§] Christoph Neinhuis,[∥,⊥] and Carsten Werner*[,†,‡,⊥]

[†]Max Bergmann Center of Biomaterials, Leibniz Institute of Polymer Research Dresden, 01069 Dresden, Germany

[‡]Research Training Group "Nano- and Biotechniques for Electronic Device Packaging", Technische Universität Dresden, 01062 Dresden, Germany

[§]Institute of Scientific Computing, Technische Universität Dresden, 01062 Dresden, Germany

[∥]Institute of Botany, Technische Universität Dresden, 01062 Dresden, Germany

[⊥]B CUBE Innovation Center for Molecular Bioengineering, Technische Universität Dresden, 01307 Dresden, Germany

Ⓢ *Supporting Information*

ABSTRACT: Springtails (Collembola) are wingless arthropods adapted to cutaneous respiration in temporarily rain-flooded habitats. They immediately form a plastron, protecting them against suffocation upon immersion into water and even low-surface-tension liquids such as alkanes. Recent experimental studies revealed a high-pressure resistance of such plastrons against collapse. In this work, skin sections of *Orthonychiurus stachianus* are studied by transmission electron microscopy. The micrographs reveal cavity side-wall profiles with characteristic overhangs. These were fitted by polynomials to allow access for analytical and numerical calculations of the breakthrough pressure, that is, the barrier against plastron collapse. Furthermore, model profiles with well-defined geometries were used to set the obtained results into context and to develop a general design principle for the most robust surface structures. Our results indicate the decisive role of the sectional profile of overhanging structures to form a robust heterogeneous wetting state for low-surface-tension liquids that enables the omniphobicity. Furthermore, the design principles of mushroom and serif T structures pave the way for omniphobic surfaces with a high-pressure resistance irrespective of solid surface chemistry.
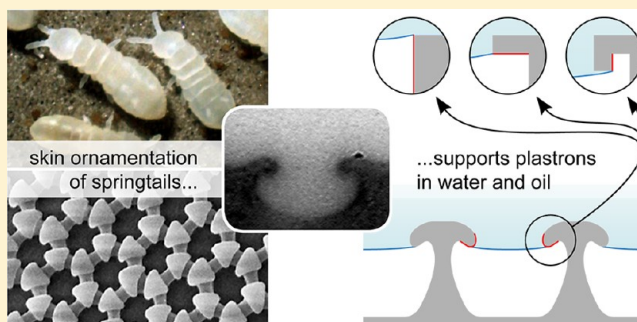
1. INTRODUCTION

Omniphobic surfaces have become a focus of interest due to their maintenance of a heterogeneous wetting state, even with very low-surface-tension liquids such as alkanes.[1−9] In a heterogeneous wetting state, the asperities of a rough surface topography sustain trapped air inside the grooves underneath a continuous liquid phase. This results in a composite interface consisting of a liquid−air and a solid−liquid interface.[10] A thermodynamically stable heterogeneous wetting state for water is usually achievable by means of a sufficiently high intrinsic contact angle, θ_Y, that should preferably be higher than 90°, and an appropriately chosen roughness.[11] Liquids with lower surface tensions than water typically have an intrinsic contact angle that is lower than 90° even on low energy surfaces such as Teflon. Here, a heterogeneous wetting state is feasible by inhibition of the liquid penetration into the grooves by implementation of surface topography elements with overhangs that were first mentioned by Herminghaus.[12] Thermodynamic analysis of wetting equilibrium states, dealing with the minimization of the Gibbs energy of a system, have already confirmed that rough surfaces with overhanging cross-sectional

profiles can maintain a heterogeneous state, even for a low θ_Y.[13−17] However, the heterogeneous wetting state is energetically metastable and can be transferred into a homogeneous wetting state by means of applied energy.[18] Thus, beyond predicting the existence of the heterogeneous wetting state, the stability against an enforced wetting transition and the dynamics of this process are of great interest, in particular, in technological applications.

The geometrical concept of omniphobic surfaces, which bases on overhanging cross-sectional profiles, has already been translated into different types of engineered rough surfaces such as porous gold surfaces,[19] certain polymer[20] or silicon oxide[5] structures, fiber mats,[2,9,21] fabrics,[4,6] pillar structures,[1−3,7,8,22,23] or hierarchical structures.[14,24] However, omniphobicity in natural surfaces is rare. Many plant surfaces show a high repellency against water droplets and a wetting resistance upon immersion into water by the formation of an air layer (called

physical gill or plastron),[25−27] but most of them are easily wetted by low-surface-tension liquids. Some attention should be drawn to springtails (Collembola) that are mainly soil-dwelling wingless arthropods (Figure 1A). The skin of these
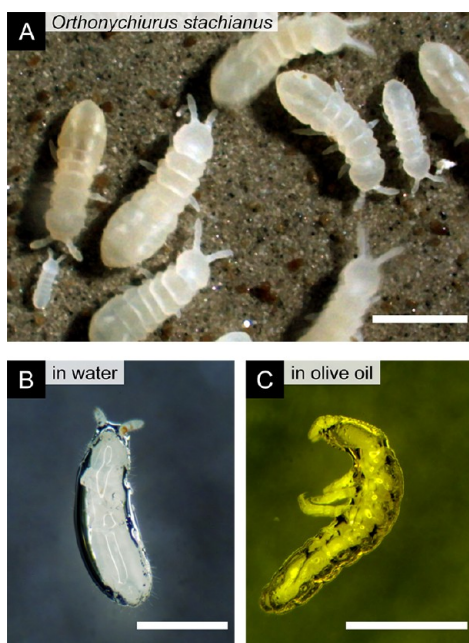
Figure 1. (A) Springtail colony of *Orthonychiurus stachianus*. (B, C) Plastron surrounding the entire animal upon immersion into (B) water and (C) olive oil. Scale bars: 1 mm.

animals exhibits omniphobicity that enables the formation of stable plastrons upon immersion into water (Figure 1B) and even into many low-surface-tension liquids such as oil (Figure 1C) or ethanol.[28] The plastron formation protects these skin breathing animals against suffocation in their often rain-flooded habitat. Furthermore, it was found that these plastrons show a resistance against collapse at elevated pressures. For instance, the plastron sustains more than 3500 hPa in water and more than 1000 hPa in olive oil. The origin of this exceptional wetting resistance is based on the hierarchically aligned micro- and nanostructures of the skin surface,[28] although a quantitative theoretical elaboration is still missing.

The objective of the present work is to understand the experimentally found wetting resistance of the springtail skins[28,29] and is organized in the following sections. In section 2, we develop an analytical approach for the determination of the breakthrough pressure that a priori affords an evidence of the wetting resistance. Furthermore, the breakthrough phenomena canthotaxis and the Laplace breakthrough are defined. In section 3, we present a numerical finite element method for computing the dynamics of an enforced wetting transition process. In subsection 4.1, we analytically calculate and discuss the wetting resistance of the springtail skin based on transmission electron micrographs of *Orthonychiurus stachianus* using polynomial fits for detailed representation of the sectional surface profiles. In subsection 4.2, we analyze the wetting resistance of model profiles that basically consist of straight lines and sharp edges. In subsection 4.3, we compare and discuss the numerical results for all considered sectional profiles with the analytical results of subsection 4.1 and 4.2 for consolidation of the presented concept.

2. ANALYTICAL THEORY

Different concepts are currently being used to describe wetting phenomena on solid surfaces. One common approach is referred to as "energy concept" that is mainly used to predict the existence of heterogeneous wetting states on rough surfaces. The free enthalpy (Gibbs energy) of the three-phase system is analyzed for minima in the energy function that correspond to possible heterogeneous and homogeneous wetting states on a certain rough surface.[17,30] Supposing a liquid droplet, these distinctive wetting states are associated to several macroscopic contact angles and contact angle hysteresis.[31,32] This means that the same droplet can have different shapes on the same solid surface in both wetting states. In this work another approach is used, which is referred to as "pressure concept".[33] This concept allows for analytical determination of the wetting resistance, that is, the robustness of the heterogeneous wetting state. Herein, the penetration of an expanding fluid into the micro- and nanoscopic grooves of rough surfaces is taken into account, until the homogeneous wetting state is achieved. Note that, both the pressure and the energy approach allow for the estimation of the wetting transition barrier. However, while the pressure concept commonly allows for analytical access in cases of solid surfaces with complex shaped geometries the energy concept essentially requires numerical models.[34]

Experimentally, the expansion of the liquid front can be initiated by a continuously increasing hydrostatic pressure inside the applied liquid phase. The resistance against a pressure-induced wetting transition can be analytically described by the Laplace's law:

$$\Delta p = \frac{2\gamma}{R} \tag{1}$$

supported by the Young's equation:

$$\cos \theta_Y = \frac{\gamma_{sg} - \gamma_{sl}}{\gamma} \tag{2}$$

where γ_{sg}, γ_{sl}, and γ are the interfacial energies of the solid−gas, the solid−liquid, and the liquid−gas phase boundary, respectively, which are related to each other by the intrinsic contact angle, θ_Y. Throughout this work, θ_Y was analytically and numerically considered in the range between 0° and 120°, which approximately corresponds to common natural surfaces and liquids.[18] The Laplace's law describes the pressure difference, Δp, across the liquid−gas interface for a certain interface curvature radius, R, that is also connected to θ_Y as will be shown below.

Figure 2 illustrates two distinctive pressure-induced wetting transition phenomena. In the initial situation (Figure 2A), a liquid phase is applied atop a circular cavity with the radius, x, and geometrical edge angle, Ψ, of the conical cross-sectional profile. Immediately after application, the liquid is sustained atop the cavity when $\Psi < \theta_Y$. We assume that the volume of the liquid phase is sufficiently large compared to the cavity radius. The curvature of the liquid−air interface inside the cavity has to be equal to the curvature of the liquid phase itself, which is very small. Consequently, the initial liquid−air interface inside the cavity is assumed to be planar and can be represented by $\Delta p = 0$.

In formulating the wetting transition conditions and the breakthrough pressure, we consider solid surfaces to be ideal (rigid, insoluble, homogeneous, non-reactive) so that any contact angle hysteresis can be neglected and the intrinsic
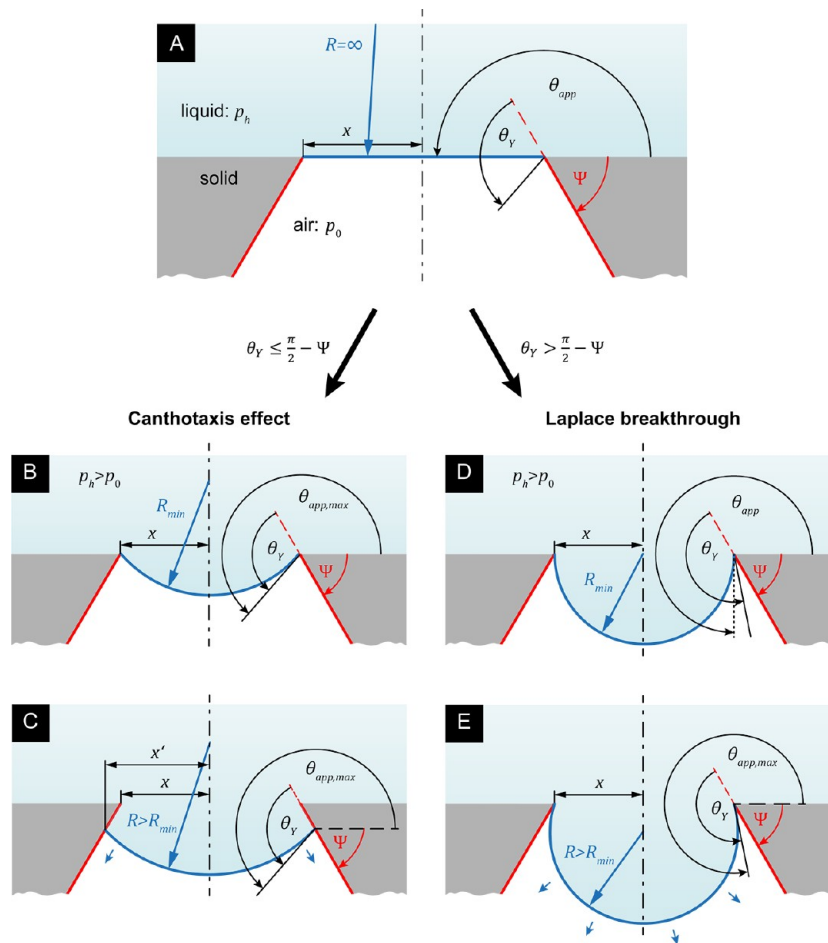
Figure 2. Illustration of two distinctive pressure-induced wetting transition phenomena. (A) Liquid phase sustained atop a circular cavity with the radius, x, and geometrical edge angle, Ψ, of a conical cross-sectional profile with intrinsic contact angle, θ_Y. (B−E) In both considered phenomena, the liquid−air interface sags into the cavity due to continuously increasing hydrostatic pressure, p_h, whereas the air pressure, p_0, is kept constant. (B) In the canthotaxis case, the critical pressure difference is achieved when the apparent contact angle, θ_{app}, of the sagging liquid−air interface becomes $\theta_Y + (\pi + \Psi)$ (eq 4). (C) The three-phase contact line immediately slides downward the cavity side-wall (symbolized by arrows). (D) The critical pressure difference in the Laplace breakthrough phenomenon is achieved when the sagging liquid−air interface forms a semicircular profile that corresponds to the minimal curvature radius, R_{min}, which corresponds to the maximal Laplace pressure across the interface. (E) The liquid front inevitably breaks through (symbolized by arrows) by further increasing hydrostatic pressure.

contact angle is the only independent variable. Throughout this work, the edge angle, Ψ, is considered on the right-hand side of the cavities. Furthermore, deformations of the liquid−air interface caused by gravitational forces can be ignored due to considerably small dimensions of the cavity (cf. Figure 4) in comparison to the capillary length of the liquid phase, $\lambda_{cap} = (\gamma/\rho g)^{1/2}$, which is ~2.7 mm for water and ~1.7 mm for hexane (ρ is the mass density and g is the gravitational constant).

A continuously increasing hydrostatic pressure, p_h, inside the liquid phase induces a sagging of the liquid−air interphase into the cavity due to the sustained pinning of the three-phase contact line at the solid edge. The sagging interface has the shape of a spherical cap with a curvature radius, R, that is given by

$$R = \frac{x}{\sin(\theta_{app} - \pi)} \tag{3}$$

where x is the distance between the three-phase contact line and the symmetry center of the cavity and θ_{app} is the apparent angle between the fluid interface and the horizon. For further simplicity, we assume that the expanding liquid front does not result in a compressed air reservoir inside the cavity ($p_0 = $

const). This can be justified by the highly permeable cuticle of the skin breathing springtails.[35] The pinning of the three-phase contact line at the edge is maintained until θ_{app} achieves a maximal value that can be described by the following geometrical boundary condition:[36,37]

$$\theta_{app,max} = \theta_Y + (\pi + \Psi) \tag{4}$$

A further increase of the hydrostatic pressure results in a downward directed sliding of the three-phase contact line along the cavity side-wall, that is, the breakthrough scenario that finally results in a homogeneous wetting state.

With regard to the critical pressure difference that induces the breakthrough scenario, two phenomena have to be distinguished. The first phenomenon is referred to as canthotaxis effect.[38] Here, the critical pressure difference directly corresponds to the geometrical boundary condition (eq 4) as illustrated in Figure 2B and C. The critical pressure difference can be calculated using eqs 1,3, and 4 and is denoted as breakthrough pressure, Δp_{break}:

$$\Delta p_{break} = p_h - p_0 = \frac{2\gamma \sin(\theta_Y + \Psi)}{x} \tag{5}$$

The other phenomenon is referred to as Laplace breakthrough and is illustrated in Figure 2D and E. Here, the sagged liquid–air interface forms a semicircular shape before the geometrical boundary condition (eq 4) is fulfilled. Thus, the semicircular shape corresponds to the minimal achievable curvature radius as well as the maximal Laplace pressure across the interface. When the hydrostatic pressure inside the liquid phase still increases, the liquid front inevitably breaks through. The breakthrough pressure is determined by the Laplace law (eq 1) with $R = x$:

$$\Delta p_{break} = p_h - p_0 = \frac{2\gamma}{x} \tag{6}$$

and consequently depends only on the surface tension of the applied liquid and the cavity radius. In sum, the robustness of a heterogeneous wetting state can be determined either by the canthotaxis effect (eq 5) or the Laplace breakthrough (eq 6). The transition between both phenomena is given by the relation between θ_Y, the intrinsic contact angle and Ψ, the edge angle:[38]

$$\text{Canthotaxis effect:} \quad \theta_Y \leq \frac{\pi}{2} - \Psi \tag{7}$$

$$\text{Laplace breakthrough:} \quad \theta_Y > \frac{\pi}{2} - \Psi \tag{8}$$

The previous approach illustrates the wetting transition for a conical-shaped cavity using the edge angle, Ψ. In addition, this angle describes the slope of the cavity side-wall that was constant ($\Psi := \text{const}$) in our first considerations. Note, that for more complex shaped cavities, such as discussed in the section 4, the slope along the cavity side-wall may change, so $\Psi := f(x)$. In general, the slope is given by the arctangent of the first derivative of the function that describes the side-wall profile.

3. NUMERICAL SIMULATIONS

In addition to the analytical methods, we performed numerical finite element method (FEM) simulations to gain insight into the dynamics of the wetting transition process with respect to all cross-sectional profiles, which are analytically discussed in this work. In contrast to the analytical studies, the numerical simulations were carried out using a two-phase flow model. To remove singularities at the three-phase contact line, a diffuse interface (phase-field) model was employed. It is based on a phase field variable, ϕ, that ranges between ± 1 in the bulk of the two fluids and varies continuously across the interface with finite thickness, d (Figure 3). Thus, the interface is not sharp, but diffuse, which is a realistic assumption in nanoscopic systems.[39] The diffuse interface model for mixtures of two immiscible and incompressible fluids leads to the following Navier–Stokes–Cahn–Hilliard equations that have been considered by several authors:[40−43]

$$\rho(\phi)(\partial_t \mathbf{u} + \mathbf{u} \cdot \nabla \mathbf{u}) = -\nabla p + \nabla \cdot (\nu \mathbf{D}) + \frac{\sigma}{\varepsilon} \mu \nabla \phi \tag{9}$$

$$\nabla \cdot \mathbf{u} = 0 \tag{10}$$

$$\partial_t \phi + \nabla \cdot (\phi \mathbf{u}) = c_{CH} \varepsilon^{-1} \nabla \cdot (B(\phi) \nabla \mu) \tag{11}$$

$$\mu = B'(\phi) - \varepsilon^2 \Delta \phi \tag{12}$$

Here $\mathbf{u}$, p, and μ are the velocity, pressure, and chemical potential, respectively. The function $B(\phi) = 1/4(\phi^2 - 1)^2$ is a double well potential, $\mathbf{D} = (\nabla \mathbf{u} + \nabla \mathbf{u}^T)$, $c_{CH} = 0.0002$ is a
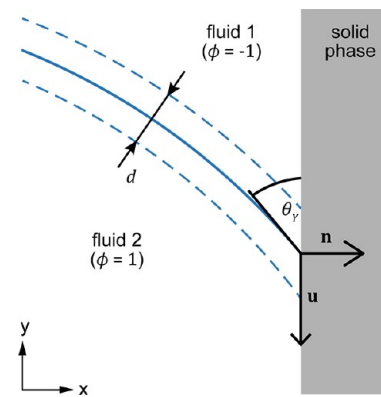
Figure 3. Dynamic contact line in a diffuse-interface framework. The phase-field variable, ϕ, represents the two fluid bulks by $\phi = \pm 1$ and the fluid–fluid interface by $\phi = 0$ (solid line). The thickness of this interface is d. The advancing of the three-phase contact line is characterized by $\mathbf{n}$ the surface normal, $\mathbf{u}$ the velocity, and θ_Y the intrinsic contact angle.

mobility constant, and $\sigma = 250$ a scaled surface tension. Furthermore, we set the density of the upper fluid $\rho(\phi = 1) = 5$ and the lower fluid $\rho(\phi = -1) = 0.1$ with a linear interpolation in between. The viscosity is $\nu = 1$, and the interface thickness is $\varepsilon = 0.005$. The capillary and Reynolds number can be calculated by the given: $Re = \rho/\nu$ that 5 and 0.1 for the upper and lower fluid, respectively, and $Ca = \nu\varepsilon/\sigma = 2 \times 10^{-5}$. Note that these numbers result in a laminar flow regime dominated by surface tension. The dominating forces of our system are hydrostatic pressure and interfacial tension. As boundary conditions, we imposed a pressure difference $\Delta p = p_{top} - p_{bottom}$ between the top and bottom boundary, which pushed the fluids downward for $\Delta p > 0$. The pressure, p_{top}, is described and increased linearly and slowly over time. Before the breakthrough, contact lines slide across surfaces at fixed contact angle conditions: The contact line movement is only driven by the increase in pressure; if we stop increasing the pressure the contact line stops moving as well. Thus, we are working in a quasi-static regime as long as no breakthrough occurs. At the remaining solid boundaries, we used the no slip condition $\mathbf{u} = 0$. Furthermore, we specified a contact angle condition, $\mathbf{n} \cdot \nabla \phi = |\nabla \phi| \cos(\theta_Y)$, to enforce the prescribed contact angle, where $\mathbf{n}$ is the surface normal.

The system of equations was solved by an FEM with a semi-implicit Euler time stepping algorithm. The adaptive finite element toolbox AMDiS[44,45] is used for discretization. The numerical results were compared to the analytical results using the determined curvature of the fluid interface and the position of the three-phase contact line for each time step. Thereby, the curvature was calculated by integrating $(3/(2\sqrt{2}\varepsilon))\mu|\nabla\phi|$ across the interface.[46]

4. RESULTS AND DISCUSSION

4.1. Surface Topography and Wetting Resistance of Springtails. Animal collection, in vitro cultivation, and sample preparation for scanning and transmission electron microscopy studies were similar as described by Helbig et al.[28] In Figure 4A, the characteristic nanoscopic skin morphology of *Orthonychiurus stachianus* is depicted. The entire skin of the animal is covered by a comb structure with hexagonally arranged cavities. Furthermore, granules are located at the intersections of the structure that finally results in a regularly arranged, but
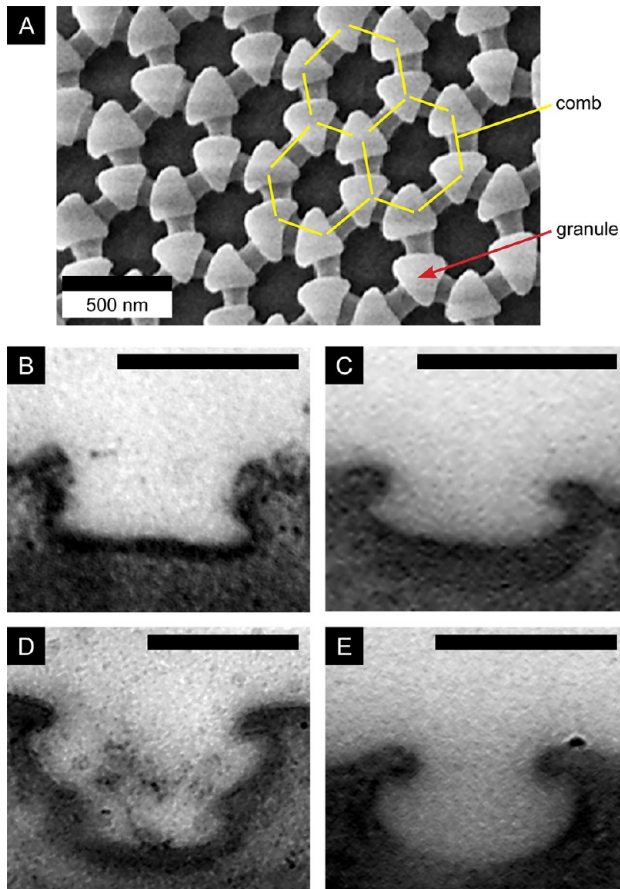
Figure 4. Skin surface topography of the springtail *Orthonychiurus stachianus*. (A) Scanning electron micrograph reveals the nanoscopic skin ornamentation with granules at the intersections of the underlying comb structure. (B–E) Different sections through the skin, taken by transmission electron microscopy, show cavities with characteristic overhanging cross-sectional profiles (scale bars: 300 nm).

complex-shaped surface structure, which is typical for springtails.[28,29,35,47] Cross-sectional images of this surface topography, taken by transmission electron microscopy, show different shapes of cavities but all exhibit overhangs at their top edges (Figure 4B–E). We suggest that the different shapes originate from different sections through the cavities. We analytically studied two distinctive cavity shapes (Figure 4B and E) to get a first impression of their wetting performance, in particular, the pressure resistance against the wetting transition from the heterogeneous to the homogeneous wetting state, that is, the plastron collapse. The overhanging part of the side-wall profiles of these cavities were fitted with polynomials $F_n(x) = \sum_{i=0}^{n} a_i x^i$ by measuring points using the open-source software *ImageJ*, v. 1.43,[48] to get access to the distinctive shapes. The polynomial fits with the highest coefficient of correlation have been chosen for further analysis (applied with *Origin*, OriginLab, v. 8.6). The origin of the coordinate system was set to be at the bottom center of each cavity. The first cavity side-wall (Figure 4B) was fitted using a fourth degree polynomial where $a_4 = 1.60 \times 10^{-4}$, $a_3 = -0.12$, $a_2 = 32.895$, $a_1 = -4035.09$, and $a_0 = 185\,224$. The polynomial is displayed as green line in Figure 5A and reflects the characteristic overhang of the cavity in the range 156 nm < x < 190 nm with a point of inflection at $x_{inf} = 175$ nm in a height of $y_{inf} = 17$ nm. The second cavity side-wall (Figure 4E) was fitted using a third degree polynomial where $a_3 = -3.14 \times$

10^{-4}, $a_2 = 0.19$, $a_1 = -37.77$, and $a_0 = 2674.80$. Here, the characteristic overhang is located in the range 140 nm < x < 260 nm with a minimum at $x_{min} = 180$ nm, a maximum at $x_{max} = 220$ nm, and the point of inflection at $x_{inf} = 201$ nm in a height of $y_{inf} = 196$ nm (Figure 5D). The local slope along the side-wall of the cavity, Ψ, can be determined by the first derivative of the polynomial:

$$\Psi = \arctan(dF_n/dx) \tag{13}$$

The maximal slope along the fitted profiles are situated in the point of inflections that gives a negative slope $\Psi(x_{inf}) = -20°$ for the first (Figure 5A) and a positive slope $\Psi(x_{inf}) = 23°$ for the second profile (Figure 5D).

Considering an applied liquid phase atop the cavity, the Laplace pressures, Δp, across the liquid–air interface in a heterogeneous wetting regime can be calculated by eqs 1, 3, and 13, which gives:

$$\Delta p(\theta_Y, x) = \frac{2\gamma \sin(\theta_Y + \arctan(dF_n/dx))}{x} \tag{14}$$

The calculations can be visualized in three-dimensional surface plots (Figure 5B and E) depending on the current x-value of the three-phase contact point and the intrinsic contact angle, θ_Y, where the characteristic shape of the plot depends on the profile polynomial. The plots are divided into a bright blue surface area for $\Delta p(\theta_Y, x) > 0$ and a dark blue surface area for $\Delta p(\theta_Y, x) < 0$. The positive and negative Laplace pressures are related to convex and concave interface curvatures with an upward- and downward-directed capillary net force, respectively. Between both areas, the contour line $\Delta p(\theta_Y, x) = 0$ represents equilibrium states with a planar liquid–air interface, when the derivative of the pressure is positive (for further details, see Appendix A). The surface plot of the first profile (Figure 5B) shows that $\Delta p(\theta_Y, x) > 0$ is only achievable for intrinsic contact angles higher than 20° due to the maximum slope $\Psi(x_{inf}) = -20°$ along the profile in the inflection point, according to eq 5. This means that applied liquids with $\theta_Y < 20°$ concerning the solid surface immediately soak the cavity without any pinning along the cavity side-wall due to a continuously downward-directed capillary net force. On the other hand, a heterogeneous wetting state is achievable for all $\theta_Y > 20°$. The yellow line in the surface plot represents the maximum Laplace pressures, that is, the breakthrough pressures, which represent the breakthrough barrier for $\Delta p_{break} > 0$. The low height of the cavity restricts the maximal achievable breakthrough pressure in the real system due to a contact of the sagging liquid–air interface with the bottom of the cavity before the theoretical maximum occurs (see scenario (a) in Figure 5A and the red shaded region in Figure 5B). The contact with the bottom of the cavity would immediately result in a homogeneous wetting state. The condition for a sagged liquid–air interface that does not contact the bottom can be given by $F_n(x) + R(\cos(\theta_Y + \Psi(x)) - 1) > 0$. This means that the sagging height of the liquid–air interface with the curvature radius, R, is smaller than the y-value of the three-phase contact point. However, assuming water as applied liquid with a surface tension of about 72 mJ/m² and an intrinsic contact angle of $\theta_Y = 110°$ gives a pressure barrier of about 4300 hPa (Figure 5C).

The surface plot of the second and more pronounced mushroom-like profile in Figure 5E shows that a pressure barrier against homogeneous wetting, that is, a positive Laplace pressure maximum, exists for all intrinsic contact angles. There
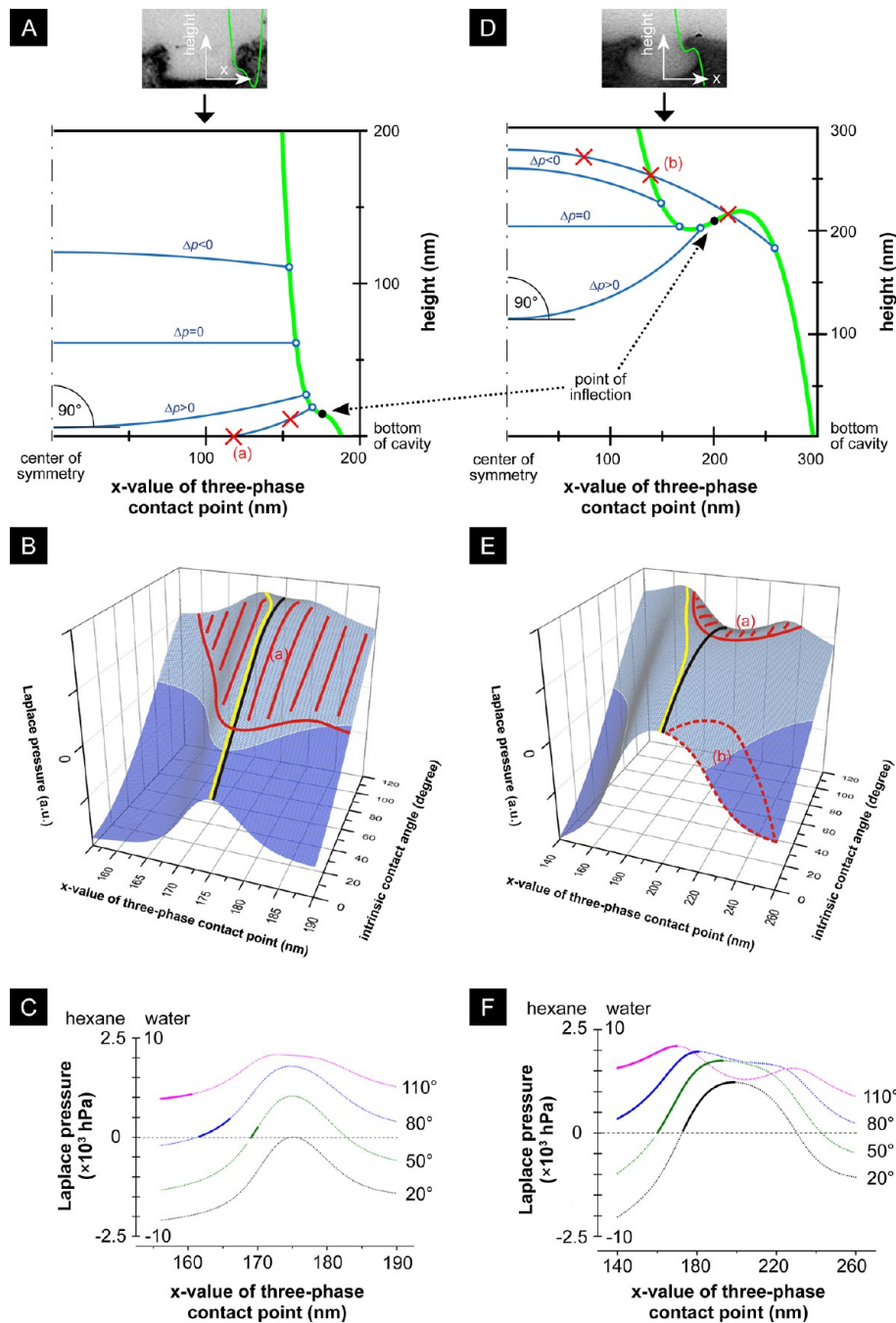
Figure 5. Analytical calculations of the Laplace pressure across the liquid–air interface for certain positions of the three-phase contact point. (A, D) Polynomial fits (green line) of two cavity profiles of *Orthonychiurus stachianus*, taken by transmission electron microscopy ((A) cf. Figure 4B; (D) cf. Figure 4E). The blue curved lines schematically represent the advancing liquid front with different Laplace pressures, Δp, across the interface. The scenarios (a) and (b) illustrate limitations given by the real system, for instance, (a) contact of the liquid–air interface with the cavity bottom and (b) physically invalid solutions. (B, E) Surface plot of the calculated Laplace pressure (eq 14) depending on the x-value of the three-phase contact point and the intrinsic contact angle, θ_Y. The bright blue surface area represents the solutions $\Delta p(\theta_Y, x) > 0$, and dark blue surface areas the solution $\Delta p(\theta_Y, x) < 0$. The yellow and the black line represent the maximal possible Laplace pressure and the position of the polynomial inflection point, respectively. The red shaded areas (a) and the area that is encased with a dotted red line (b) represent physically invalid solutions. (C, F) Curves for different intrinsic contact angles that represent calculated Laplace pressures for hexane and water with surface tensions of ~18 and ~72 mJ/m², respectively. The thick solid part of the curves represents the physically valid and relevant positive segments of the solutions.

even exist two positive maxima for $\theta_Y > 67°$, but the value of the first maximum (that is located before the point of inflection) is always higher than the second maximum (that is located after the point of inflection) due to the higher interface curvature in the first maximum. Therefore, the first Laplace pressure maximum can be considered as the actual

breakthrough pressure. In contrast to the first considered profile above, the red shaded area (scenario (a) in Figure 5D), which represents the contact of the sagged liquid–air interface with the bottom of the cavity, does not cut out any values of the maximum Laplace pressure (yellow line in Figure 5E). On the other hand, the area that is enclosed by a dashed red line also
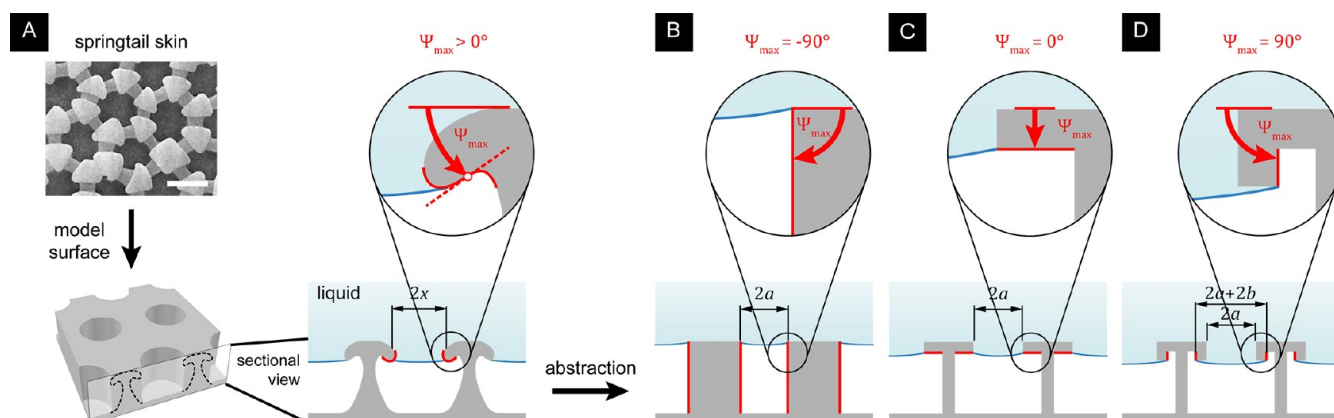
Figure 6. Geometrical models based on nanoscopic surfaces structures of *Orthonychiurus stachianus*. (A) Simplified model surface: a comb structure consisting of hexagonally arranged cavities that is based on a scanning electron micrograph showing the nanoscopic springtail skin morphology (cf. Figure 4A); scale bar: 500 nm. In the sectional view, a complex shaped profile with overhangs at the top edges suggests the shape of small granules. The maximum slope of the profile is depicted by Ψ_{max} that is higher than 0°. The current diameter of the applied liquid front inside the cavity is given by 2x. (B–D) Geometrical abstraction of the complex shaped profile into cavities with (B) straight walls where $\Psi_{max} = -90°$ and the diameter is 2a, (C) T-shaped profiles where $\Psi_{max} = 0°$ and the diameter is 2a, and (D) T-shaped profiles with serifs where $\Psi_{max} = 90°$, the diameter is 2a, and the width of the serif is b.
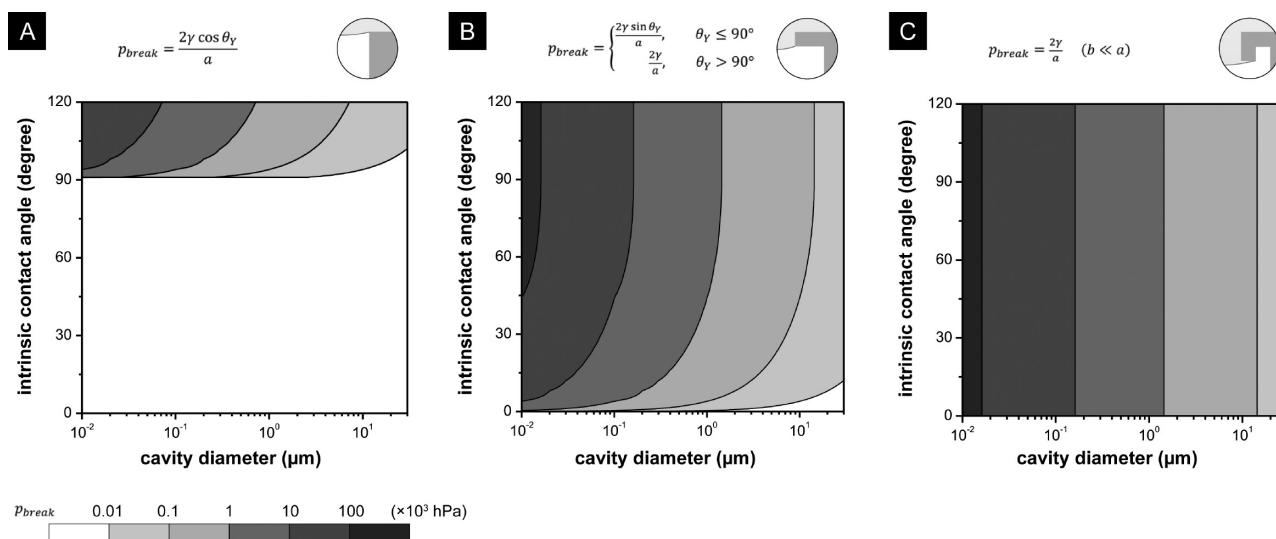
Figure 7. Contour plot of calculated breakthrough pressures, p_{break}, displaying the resistance against wetting transition for three distinctive types of model structures (cf. Figure 6B–D). Calculations were performed for water ($\gamma \sim 72$ mJ/m^2) and depend on cavity diameter, 2a, and intrinsic contact angle, θ_Y. (A) Cavity with straight side-walls. The wetting transition occurs as canthotaxis breakthrough (eqs 5 and 7). (B) Cavity with T-shaped sectional profile. The wetting transition occurs for $\theta_Y \leq 90°$ as canthotaxis breakthrough (eqs 5 and 7) and for $\theta_Y > 90°$ as Laplace breakthrough (eqs 6 and 8). (C) Cavity with serif T-shaped sectional profile under consideration that the serif width is much smaller than the diameter of the cavity. The wetting transition occurs as Laplace breakthrough (eqs 6 and 8).

represents physically invalid values. Here, for considered three-phase contact points $x > x_{inf}$, the polynomial profile was touched or crossed by the corresponding virtual liquid–air interface more than one time, which typically occurs for a low θ_Y as shown in scenario (b) in Figure 5D. For explanation, each pressure value corresponds to a certain curvature radius that is related with a certain virtual circle $(x' - x_m)^2 + (y' - y_m)^2 = R^2$, with $x_m = 0$ and y_m as the coordinates of the circle center. Therefore, the invalid values can be found numerically in $(x')^2 + (F_n(x') - y_m(\theta_Y, x))^2 = (R(\theta_Y, x))^2$, by searching for $x' \neq x$ that solve the equation in the here considered profile range for $x > x_{inf}$. The array of curves in Figure 5F represents the calculated Δp for certain values of θ_Y, in particular, for hexane and water with surface tensions of ~18 and ~72 mJ/m^2, respectively. To give some representative values, for an intrinsic

contact angle of about 20° in case of hexane or 100° in case of water the maximal Laplace pressures are about 1000 hPa and 9000 hPa, respectively. Note, that the surface tension scales the value of the Laplace pressure but does not change either the shape of the surface plot nor the zero-crossing line for $\Delta p(\theta_Y, x) = 0$ in the equilibrium state.

4.2. Wetting Resistance on Model Profiles.

Three distinctive model profiles, which are illustrated in Figure 6, were studied in order to elucidate the wetting resistance of overhanging structures more clearly. The developed geometrical model is based on a transition from straight side-walls to an abstract mushroom-like serif T-shape cross-sectional profile. This transition enabled a stepwise increase of the profile complexity. The maximum occurring slope (regarding the right part of the cavity) is −90° for straight walls (Figure 6B), 0° for
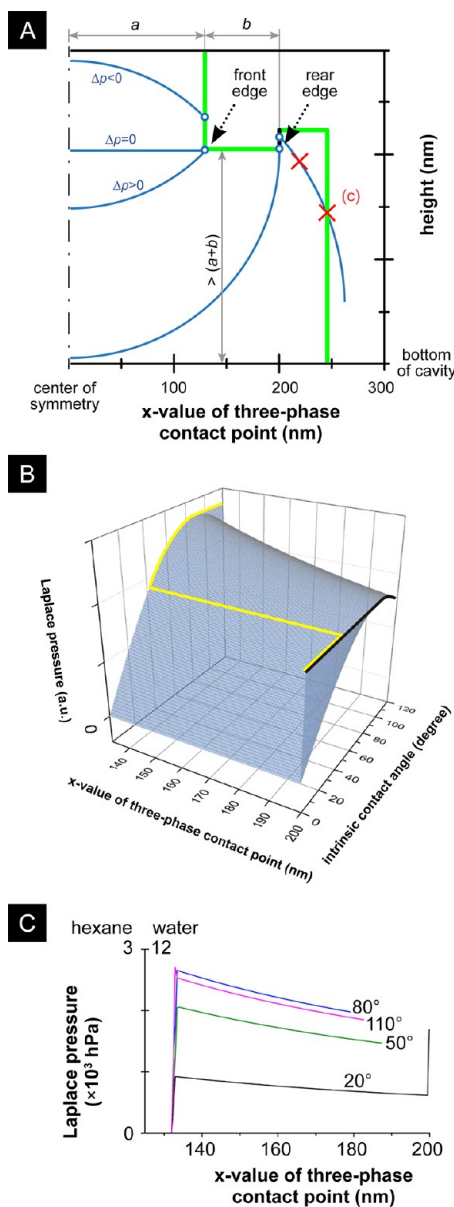
Figure 8. Analytical calculations of the Laplace pressure across liquid−air interface for a serif T-shaped profile with b/a ratio of 0.5. (A) Sectional profile of the serif T-shaped structure. The blue curved lines schematically represent the advancing liquid front with different Laplace pressures, Δp, across the interface. The scenario (c) illustrates a physical limitation given by the contact of the liquid−air interface with the inner cavity side wall. (B) Surface plot of the calculated Laplace pressure (eq 14) depending on x-value of the three-phase contact point and the intrinsic contact angle. The yellow and the black line represent the breakthrough pressure and the position of the rear edge of the serif, respectively. (C) Curves for different intrinsic contact angles that represent calculated Laplace pressures for hexane and water with surface tensions of ∼18 and ∼72 mJ/m², respectively.

T-shaped profiles (Figure 6C), and +90° for T-shaped profiles with serifs (Figure 6D). The qualitative principles of the model profiles and their increased resistance against wetting are illustrated in Figure 7. The values were calculated using the surface tension of water, but the general trend is qualitatively similar for all liquids. A heterogeneous wetting state in the case of straight walls is only achievable for intrinsic contact angles higher than 90° (Figure 7A). T-shape profiles with a maximal
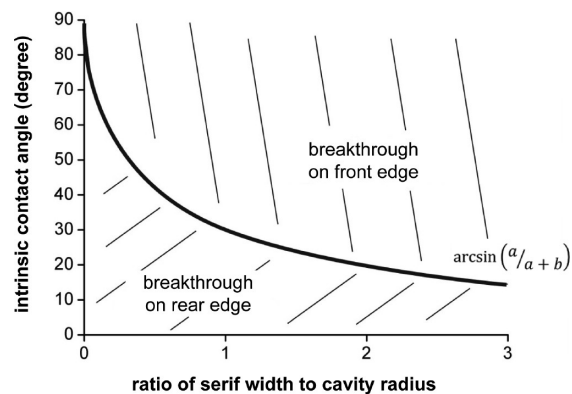
Figure 9. Ratio of serif width to cavity radius that determines at which serif edge the breakthrough for different intrinsic contact angles occurs. For contact angles higher than 90°, the breakthrough occurs always on the front edge.

slope of 0° can already resist a full wetting against liquids that adopt intrinsic contact angles close to 0° (Figure 7B). There exists a transition at $\theta_Y = 90°$ between the canthotaxis and the Laplace breakthrough according to eqs 7 and 8. For $\theta_Y > 90°$, the breakthrough pressure scales only with the surface tension, γ, of the applied liquid and inversely proportional with the cavity radius, a, regardless of the intrinsic contact angle. On the other hand, the pressure resistance sinks for $\theta_Y < 90°$ with decreasing θ_Y. In a real system, which exhibits a maximal slope of 0°, it may occur that for very small intrinsic contact angles the breakthrough barrier is small enough to be overcome by pressure fluctuations such as acoustical or mechanical vibrations, which would result in an insufficient resistance against wetting. Consequently, the resistance of T-shaped profiles is less robust for very small intrinsic contact angles. A further extension of pressure resistant sectional profiles are serif T structures (cf. Figure 6D) that exhibit a maximal slope of 90°. In a first consideration, we assume that the width of the serif, b, is small compared to the radius of the cavity, a, that gives $a \approx a + b$. The breakthrough pressure has the same value for all θ_Y due to the effect that the maximum Laplace pressure will always occur when the liquid interface forms a semicircular shape corresponding to the Laplace breakthrough (Figure 7C). Thus, the T-shaped profiles with serifs provide a stable heterogeneous wetting state irrespective of the solid and liquid chemistries for small cavity dimensions.

We performed further analysis to gain a closer look into this type of profile. We chose spatial dimension of such a T-shaped profile with serifs similar to what has been found on the springtail skin. Thus, the distance $a + b$ was chosen to be 200 nm (Figure 8A). The height of the serif inside the cavity is considered to be higher than $a + b$ to inhibit the contact between the sagged liquid−air interface and the bottom of the cavity before the maximal Laplace pressure occurs. The surface plot in Figure 8B does not display any negative values of the Laplace pressure that indicate a pressure barrier against homogeneous wetting for all θ_Y, according to the displayed results in Figure 7C. However, the surface plot exhibits a discontinuity along the profile at the first and the second pinning position of the three-phase contact line, that is, the front and rear edge of the serif, respectively. After depinning at the front edge, the three-phase contact line is sliding between both edges with decreasing liquid−air interface curvature. Consequently, the maximal Laplace pressure for each θ_Y is
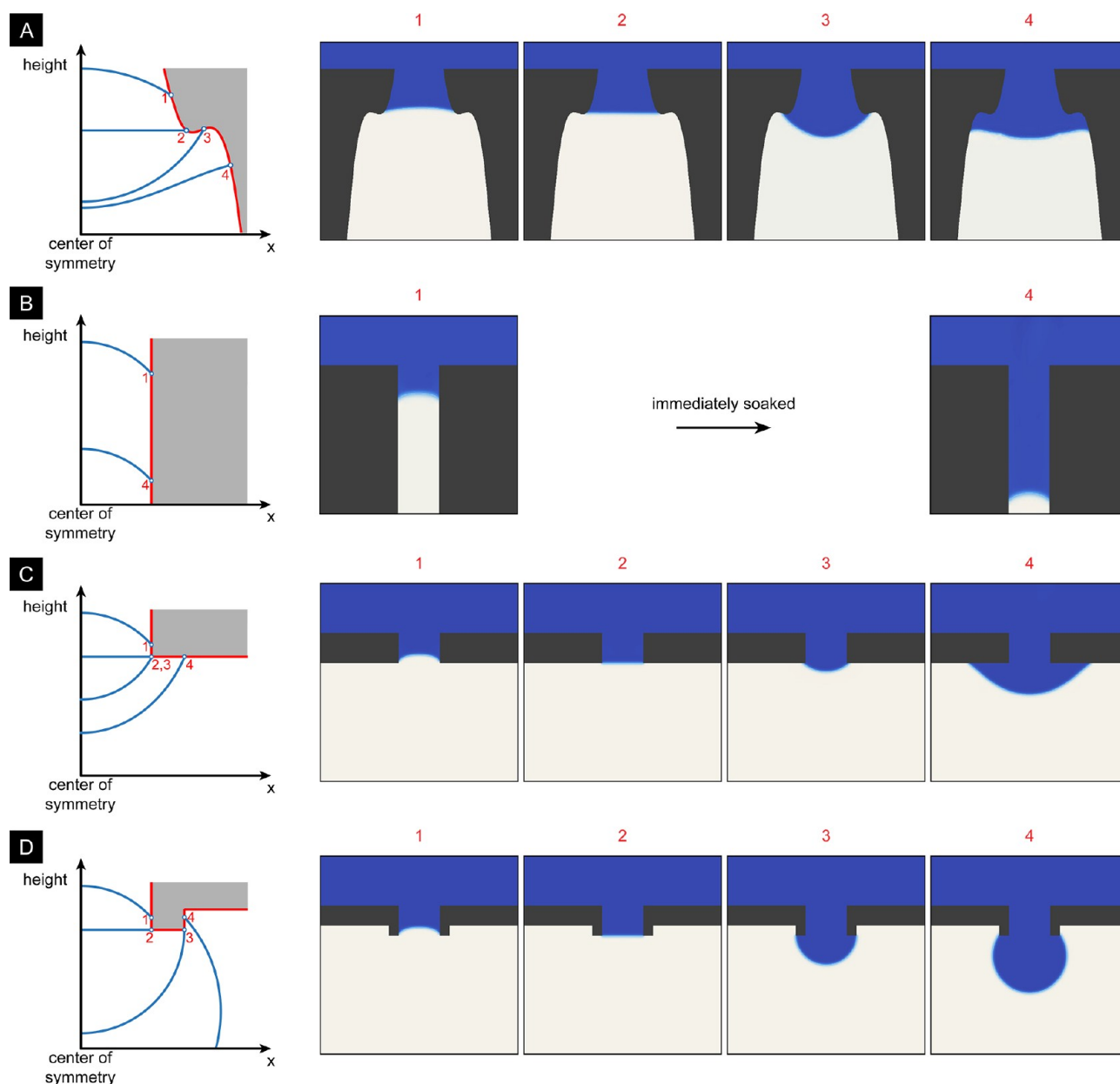
Figure 10. Numerical simulations displaying the pressure-induced wetting transition dynamics inside cavities with different cross-sectional profiles and an intrinsic contact angle of 40°. Each panel consists of a scheme on the left-hand side, which illustrates the advancing of the sagging liquid−air interface, and certain characteristic intermediate steps (that do not necessarily correspond to the same time steps in the simulations) on the right-hand side. Step 1 shows the initial partial filling of the cavities by the applied liquid. Step 2 reveals the planar interface in equilibrium state inside the cavity. Step 3 represents the maximal achievable curvature of the fluid interface corresponding to the maximal Laplace pressure, that is, the breakthrough pressure. Step 4 shows the advanced wetting that finally results in a filled cavity. (A) Natural mushroom profile that corresponds to polynomial in Figure 5D. (B) Cavity with straight side-wall profile that was immediately wetted without any applied pressure. (C) Cavity with T-shaped sectional profile. (D) Cavity with serif T-shaped sectional profile with ratio of serif width to cavity radius of 0.5.

located either on the front or on the rear edge. The array of curves in Figure 8C for certain θ_Y shows that the maximal Laplace pressure for 50°, 80°, and 110° is already achieved at the front edge whereas for 20° the maximal Laplace pressure is achieved in the second pinning position on the rear edge. The condition (Figure 9) that defines the position of the global pressure barrier for each θ_Y depends on the ratio of serif width, b, and cavity diameter, a, and can be calculated by $\theta^* = \arcsin(a/(a + b)) = \arcsin(1/(1 + (b/a)))$. This condition evolves for $\theta_Y < 90°$ from the comparison of the minimal curvature radius on the front edge, which is $a/\sin(\theta_Y)$, and on the rear edge, which is $a + b$. For $\theta_Y \geq 90°$, the maximum

pressure occurs always on the front edge. Consequently, for $\theta_Y < 90°$, the maximal Laplace pressure occurs at the front edge for $\theta_Y > \theta^*$ and at the rear edge for $\theta_Y < \theta^*$. In sum, T-shaped profiles with serifs enable a heterogeneous wetting state irrespective of the solid surface chemistry and even of the liquid surface tension. Varying lateral dimensions of the serif structure, represented by different ratios b/a, will not change its overall behavior due to the remaining qualitative shape of the surface plot in Figure 8B. For instance, a T-shaped profile that is given in Figure 8A can resist a homogeneous wetting up to 1800 hPa for hexane ($\gamma \approx 18$ mJ/m^2) and an arbitrary chosen intrinsic contact angle of only 10°.
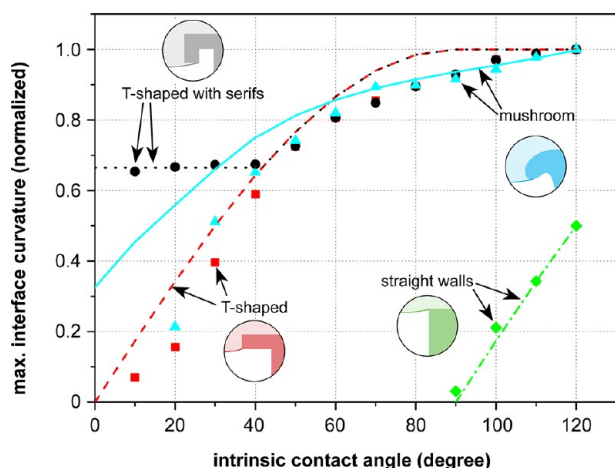
Figure 11. Maximally determined interface curvature (normalized) by numerical simulations (scatters) and analytical calculations (lines) for different cross-sectional profiles (cf. Figure 10) depending on the intrinsic contact angle. These curvatures directly correspond to the maximal achievable Laplace pressure, i.e., the breakthrough pressure.

4.3. FEM-Simulation of Wetting Dynamics. Numerical simulations were performed to consolidate our analytical results using the diffuse interface approach for two phase flow. In addition, these simulations give an insight into the actual dynamics of the wetting transition process concerning the different profiles, which were analytically analyzed in the sections 4.1 and 4.2. In Figure 10, the pressure-induced wetting transition is illustrated for an intrinsic contact angle of 40° by certain characteristic intermediate steps (that do not necessarily correspond to the same time steps in the different simulations; for supplementary movies M1−M4, see the Supporting Information). Step 1 is characterized by a concave fluid interface with a downward-directed capillary net force that leads to an initial partial filling of the cavities by the applied liquid. Step 2 shows the planar interface in equilibrium state inside the cavity. Step 3 represents the maximal achievable curvature of the fluid interface corresponding to the maximal Laplace pressure, that is, the breakthrough pressure. Step 4 shows the advanced wetting that would finally result in a filled cavity, that is, the homogeneous wetting state. Obviously, all considered profiles with overhangs can sustain a heterogeneous wetting state on hydrophilic solid surfaces. Only the cavity with straight walls without any overhang was immediately soaked by the applied liquid phase.

Furthermore, the dynamics for intrinsic contact angles between 10° and 120° in steps of 10° were computed concerning the presented profiles. The breakthrough scenario was again defined as the moment where the highest positive curvature of the sagged fluid interface was achieved. The determined normalized curvatures are plotted along with the analytical results in Figure 11. The pressure-induced resistance against a wetting transition significantly depends on the type of profile. The highest resistance, particularly in the case of a low θ_Y, is achievable using T-shaped profiles featuring serifs, which is in line with our analytical results. Structures with straight walls afford a heterogeneous wetting state for intrinsic contact angles higher than 90°. The robustness of such type of structure increases with increasing θ_Y, but is always lower than the robustness of structures with overhangs such as the mushroom structures and the sans-serif and the serif T structures. In particular, sans-serif and serif T structures exhibit the same

robustness for $\theta_Y > 90°$, which is determined by the Laplace breakthrough.

The overall trend is similar for both the numerical and the analytical approach with the exception of some minor differences due to distinctive assumptions of the fluid interface dimensions. The interface in the numerical approach is not sharp, but has a certain thickness in contrast to the analytical approach. This suggests that the pinning of the three-phase contact point is not located at a certain point of the edge on the profile but is rather advancing around the edge during the "pinning event" (for further details, see Appendix B). Consequently, the local position of the three-phase contact point varies close to the edge and has a direct influence on the maximal achievable interface curvature. This effect becomes, in a qualitative manner, realistic for real nano- and microscopic structures that do not have ideally sharp edges[38] (Figure B1D).

5. CONCLUSIONS

The robustness of plastrons formed upon immersion of springtails into water or even low-surface tension liquids is elucidated. A clear depiction of the origin of the wetting resistance has been given by analytical calculations and numerical finite element computations. The results show good consistency with experimentally determined pressure values[28] and expand the understanding in field of wetting robustness of overhanging surface structures. In principle, mushroom-shaped profiles, which were proven on springtail skin, often exhibit positive slopes along the profile as structural requirement for high-pressure resistance even for low intrinsic contact angles. Further analysis of three model profiles supported this finding. It was found that the Laplace breakthrough is irrespective to the intrinsic contact angle, that is, the solid material parameter, and depends only on the lateral cavity dimensions and the surface tension of the applied liquid. In particular, the T-shaped profile with slim serifs exhibited a robust wetting resistance even for low intrinsic contact angles in contrast to often discussed T-shaped profiles.[1−3,7,17] There is no sense to increase the maximal slope higher than 90°, which may lead to a snail profile at the cavity edge, due to the already obtained robust heterogeneous wetting state of serif T structures for all intrinsic contact angles that can be only overcome by Laplace breakthrough. Consequently, from the topographical point of view, a further improvement of the profile shape for a higher wetting resistance may not be achievable. On the other hand, the smooth mushroom-shaped profile probably enables a better dewetting process compared to the serif T structure with sharp edges for low contact angles.

In reality, microfabricated surface structures do not have perfect sharp edges, but always show some smoothness that influences the pinning behavior.[38] Thus, the numerical FEM-simulations based on a diffuse liquid−gas interface may afford the correction of the analytically calculated breakthrough pressure due to blurring edge effects.

■ APPENDIX A. EQUILIBRIUM STATES INSIDE CIRCULAR CAVITIES WITH OVERHANGS DESCRIBED BY POLYNOMIALS

The three-phase contact line position of an equilibrium state, which is characterized by a planar liquid−air interface, inside a circular cavity with a sectional profile that can be described by a polynomial of the type $F_n(x) = \Sigma_{i=0}^{n} a_i x^i$, can be determined by

$$\Delta p(\theta_Y, x_i) = \frac{2\gamma \sin\left(\theta_Y + \arctan\left(\frac{dF_n}{dx}\Big|_{x_i}\right)\right)}{x_i} = 0 \tag{A1}$$

with the following boundary condition:

$$\frac{d(\Delta p)}{dx}\Big|_{x_i} = 2\gamma \left(\frac{\cos\left(\theta_Y + \arctan\left(\frac{dF_n}{dx}\right)\right)\frac{d^2 F_n}{dx^2}}{x\left(1 + \left(\frac{dF_n}{dx}\right)^2\right)} \right.$$

$$\left. - x^2 \sin\left(\theta_Y + \arctan\left(\frac{dF_n}{dx}\right)\right) \right)$$

$$> 0 \tag{A2}$$

■ APPENDIX B. ADVANCEMENT OF A DIFFUSE INTERFACE AROUND A SHARP EDGE IN NUMERICAL SIMULATIONS

At sharp edges on a solid substrate, the surface normal, n, discontinuously changes, which leads to pinning effects of a three-phase contact line. Considering a sharp water−air interface with thickness approaching zero, the three-phase contact line is sustained at the edge until eq 4 is fulfilled. On the other hand, a diffuse interface between two phase fields, ϕ, with bulk values of ± 1 that has a finite thickness, d, and a phase field gradient, $\nabla\phi$, does not stay in a certain point during pinning at the edges, but is rather advancing around this edge while the phase field gradient passes by the edge. In other words, the pinning of such an interface starts when the front side of the interface reaches the edge and comes to an end when the backside of the interface leaves the edge. Consequently, the spatial position of the fluid−fluid interface ($\phi = 0$) varies during the pinning and depends on the interface curvature and the interface thickness (Figure B1A−C). In particular, this results in a broadening of the bases diameter of the maximal sagging interface before breakthrough by the term Δx_{break}:

$$\Delta x_{break} = d_{0.95}/2\sin\theta_Y, \quad \theta_Y \leq 90°, \quad \text{and}$$

$$\phi \text{ from } -0.95 \text{ to } +0.95 \tag{B1}$$

with the finite thickness of the interface, $d_{0.95} = \sqrt{2}\varepsilon \arctan$ 0.95,[46] and the intrinsic contact angle, θ_Y. Thus, the broadening effect has a direct influence on the maximal achievable interface curvature that leads to lower pressure resistance compared to the analytically determined values (Figure 11). Furthermore, the diffuse interface model behaves similar to a sharp interface model advancing along a rounded edge (Figure B1D) that is more realistic for real applications.[38]

■ ASSOCIATED CONTENT

Ⓢ Supporting Information

Supplementary movies M1−M4 demonstrating the fluid movements including advancing and pinning states related to the simulation results of Figure 10. This material is available free of charge via the Internet at http://pubs.acs.org.
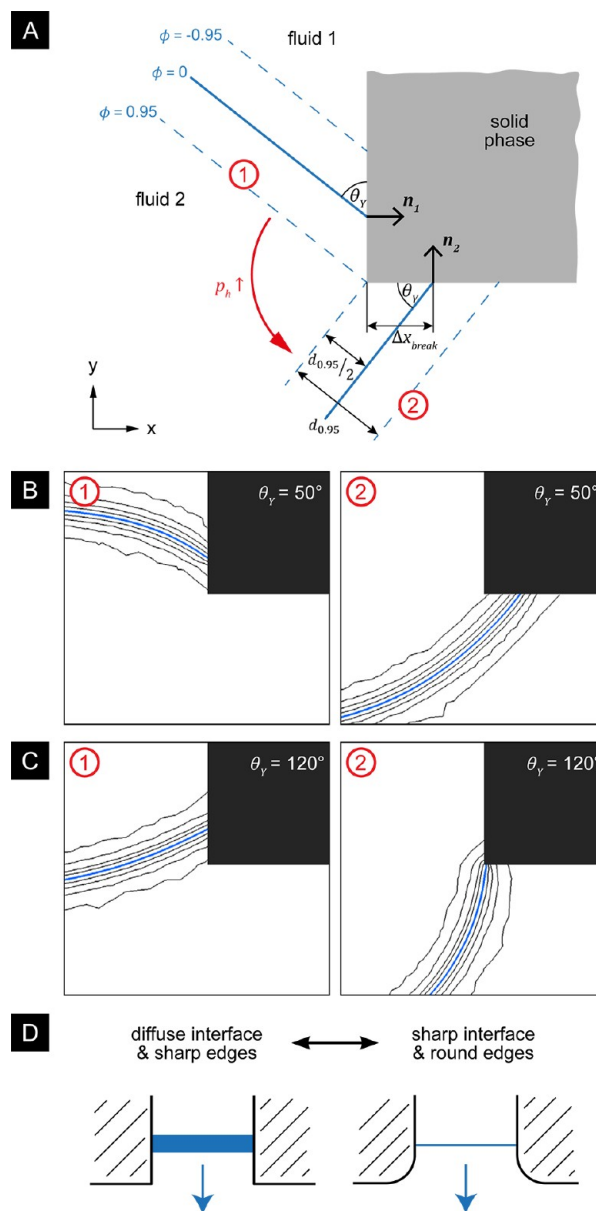
Figure B1. Advancement of diffuse interface around sharp edge. (A) In the diffuse interface model, the advancing fluid interface with the finite thickness, $d_{0.95}$, is moving around a sharp edge. In the breakthrough scenario, the base diameter of the sagged fluid interface is broadened by the term Δx_{break} compared to the diameter at the edge. The intermediate steps 1 and 2 represent the start and the end of the "pinning event", respectively. (B,C) The contour plots of the interface (range of ϕ: −0.95, −0.75, −0.5, −0.25, 0 (blue solid line), 0.25, 0.5, 0.75, 0.95) are given for both intermediate steps in the numerical simulations and the intrinsic contact angles, θ_Y, of (B) 50° and (C) 120°. (D) The diffuse interface model in combination with sharp edges behaves like a sharp interface model advancing along a rounded edge.

■ AUTHOR INFORMATION

Corresponding Author
*E-mail: werner@ipfdd.de. Phone: +49 351 4658 531. Fax: +49 351 4658 533.

Author Contributions
[#]These authors contributed equally.

■ **REFERENCES**

(1) Tuteja, A.; Choi, W.; Ma, M. L.; Mabry, J. M.; Mazzella, S. A.; Rutledge, G. C.; McKinley, G. H.; Cohen, R. E. Designing superoleophobic surfaces. *Science* **2007**, *318*, 1618−1622.

(2) Tuteja, A.; Choi, W.; Mabry, J. M.; McKinley, G. H.; Cohen, R. E. Robust omniphobic surfaces. *Proc. Natl. Acad. Sci. U.S.A.* **2008**, *105*, 18200−18205.

(3) Ahuja, A.; Taylor, J. A.; Lifton, V.; Sidorenko, A. A.; Salamon, T. R.; Lobaton, E. J.; Kolodner, P.; Krupenkin, T. N. Nanonails: A simple geometrical approach to electrically tunable superlyophobic surfaces. *Langmuir* **2008**, *24*, 9−14.

(4) Choi, W.; Tuteja, A.; Chhatre, S.; Mabry, J. M.; Cohen, R. E.; McKinley, G. H. Fabrics with Tunable Oleophobicity. *Adv. Mater.* **2009**, *21*, 2190−2195.

(5) Ramos, S. M. M.; Benyagoub, A.; Canut, B.; Jamois, C. Superoleophobic Behavior Induced by Nanofeatures on Oleophilic Surfaces. *Langmuir* **2010**, *26*, 5141−5146.

(6) Chhatre, S. S.; Choi, W.; Tuteja, A.; Park, K. C.; Mabry, J. M.; McKinley, G. H.; Cohen, R. E. Scale Dependence of Omniphobic Mesh Surfaces. *Langmuir* **2010**, *26*, 4027−4035.

(7) Dufour, R.; Harnois, M.; Coffinier, Y.; Thomy, V.; Boukherroub, R.; Senez, V. Engineering Sticky Superomniphobic Surfaces on Transparent and Flexible PDMS Substrate. *Langmuir* **2010**, *26*, 17242−17247.

(8) Im, M.; Im, H.; Lee, J.; Yoon, J.; Choi, Y. Analytical Modeling and Thermodynamic Analysis of Robust Superhydrophobic Surfaces with Inverse-Trapezoidal Microstructures. *Langmuir* **2010**, *26*, 17389−17397.

(9) Choi, G.-R.; Park, J.; Ha, J.-W.; Kim, W.-D.; Lim, H. Superamphiphobic Web of PTFEMA Fibers via Simple Electro-spinning Without Functionalization. *Macromol. Mater. Eng.* **2010**, *295*, 995−1002.

(10) Cassie, A.; Baxter, S. Wettability of porous surfaces. *Trans. Faraday Soc.* **1944**, *40*, 546−551.

(11) Bico, J.; Thiele, U.; Quéré, D. Wetting of textured surface. *Colloids Surf., A* **2002**, *206*, 41−46.

(12) Herminghaus, S. Roughness-induced non-wetting. *Europhys. Lett.* **2000**, *52*, 165−170.

(13) Liu, J.; Feng, X.; Wang, G.; Yu, S. Mechanisms of superhydrophobicity on hydrophilic substrates. *J. Phys.: Condens. Matter* **2007**, *19*, 356002 (12pp).

(14) Nosonovsky, M. Multiscale roughness and stability of superhydrophobic biomimetic interfaces. *Langmuir* **2007**, *23*, 3157−3161.

(15) Marmur, A. From hygrophilic to superhygrophobic: Theoretical conditions for making high-contact-angle surfaces from low-contact-angle materials. *Langmuir* **2008**, *24*, 7573−7579.

(16) Patankar, N. A. Hydrophobicity of Surfaces with Cavities: Making Hydrophobic Substrates from Hydrophilic Materials? *J. Adhes. Sci. Technol.* **2009**, *23*, 413−433.

(17) Xue, Y.; Chu, S.; Lv, P.; Duan, H. Importance of Hierarchical Structures in Wetting Stability on Submersed Superhydrophobic Surfaces. *Langmuir* **2012**, *28*, 9440−9450.

(18) Wenzel, R. Resistance of solid surfaces to wetting by water. *Ind. Eng. Chem.* **1936**, *28*, 988−994.

(19) Abdelsalam, M.; Bartlett, P.; Kelf, T.; Baumberg, J. Wetting of regularly structured gold surfaces. *Langmuir* **2005**, *21*, 1753−1757.

(20) Dong, W.; Zhou, Y.; Yan, D.; Mai, Y.; He, L.; Jin, C. Honeycomb-Structured Microporous Films Made from Hyper-branched Polymers by the Breath Figure Method. *Langmuir* **2009**, *25*, 173−178.

(21) Ma, M.; Hill, R. M.; Rutledge, G. C. A Review of Recent Results on Superhydrophobic Materials Based on Micro- and Nanofibers. *J. Adhes. Sci. Technol.* **2008**, *22*, 1799−1817.

(22) Cao, L. L.; Hu, H. H.; Gao, D. Design and fabrication of micro-textures for inducing a superhydrophobic behavior on hydrophilic materials. *Langmuir* **2007**, *23*, 4310−4314.

(23) Wang, J.; Liu, F.; Chen, H.; Chen, D. Superhydrophobic behavior achieved from hydrophilic surfaces. *Appl. Phys. Lett.* **2009**, *95*, 084104 (3pp).

(24) Bhushan, B.; Jung, Y.; Koch, K. Micro-, nano-and hierarchical structures for superhydrophobicity, self-cleaning and low adhesion. *Philos. Trans. R. Soc., A* **2009**, *367*, 1631−1672.

(25) Neinhuis, C.; Barthlott, W. Characterization and distribution of water-repellent, self-cleaning plant surfaces. *Ann. Bot.* **1997**, *79*, 667−677.

(26) Koch, K.; Bhushan, B.; Jung, Y.; Barthlott, W. Fabrication of artificial Lotus leaves and significance of hierarchical structure for superhydrophobicity and low adhesion. *Soft Matter* **2009**, *5*, 1386−1393.

(27) Pedersen, O.; Rich, S.; Colmer, T. Surviving floods: leaf gas films improve O2 and CO2 exchange, root aeration, and growth of completely submerged rice. *Plant J.* **2009**, *58*, 147−156.

(28) Helbig, R.; Nickerl, J.; Neinhuis, C.; Werner, C. Smart Skin Patterns Protect Springtails. *PLoS One* **2011**, *6*, e25105.

(29) Hensel, R.; Helbig, R.; Aland, S.; Voigt, A.; Neinhuis, C.; Werner, C. Tunable nano-replication to explore the omniphobic characteristics of springtail skin. *NPG Asia Mater.* **2013**, *5*, e35.

(30) Marmur, A. Wetting on hydrophobic rough surfaces: to be heterogeneous or not to be? *Langmuir* **2003**, *19*, 8343−8348.

(31) Marmur, A. Underwater superhydrophobicity: theoretical feasibility. *Langmuir* **2006**, *22*, 1400−1402.

(32) Marmur, A. Contact-angle hysteresis on heterogeneous smooth surfaces: theoretical comparison of the captive bubble and drop methods. *Colloids Surf., A* **1998**, *136*, 209−215.

(33) Zheng, Q. S.; Yu, Y.; Zhao, Z. H. Effects of hydraulic pressure on the stability and transition of wetting modes of superhydrophobic surfaces. *Langmuir* **2005**, *21*, 12207−12212.

(34) Savoy, E. S.; Escobedo, F. A. Simulation Study of Free-Energy Barriers in the Wetting Transition of an Oily Fluid on a Rough Surface with Reentrant Geometry. *Langmuir* **2012**, *28*, 16080−16090.

(35) King, P. E.; Pugh, P. J. A.; Fordy, M. R.; Love, N.; Wheeler, S. A. A comparison of some environmental adaptations of the littoral collembolans *Anuridella marina* (Willem) and *Anurida maritima* (Guérin). *J. Nat. Hist.* **1990**, *24*, 673−688.

(36) Oliver, J. F.; Huh, C.; Mason, S. G. Resistance To Spreading of Liquids By Sharp Edges. *J. Colloid Interface Sci.* **1977**, *59*, 568−581.

(37) Extrand, C. W.; Moon, S. I. Contact angles on spherical surfaces. *Langmuir* **2008**, *24*, 9470−9473.

(38) Berthier, J.; Loe-Mie, F.; Tran, V.; Schoumacker, S.; Mittler, F.; Marchand, G.; Sarrut, N. On the pinning of interfaces on micropillar edges. *J. Colloid Interface Sci.* **2009**, *338*, 296−303.

(39) Jacqmin, D. Contact-line dynamics of a diffuse fluid interface. *J. Fluid Mech.* **2000**, *402*, 57−88.

(40) Aland, S.; Voigt, A. Benchmark computations of diffuse interface models for two-dimensional bubble dynamics. *Int. J. Numer. Methods Fluids* **2012**, *69*, 747−761.

(41) Feng, X. Fully Discrete Finite Element Approximations of the Navier−Stokes−Cahn-Hilliard Diffuse Interface Model for Two-Phase Fluid Flows. *SIAM J. Numer. Anal.* **2006**, *44*, 1049−1072.

(42) Jacqmin, D. Calculation of two-phase Navier-Stokes flows using phase-field modeling. *J. Comput. Phys.* **1999**, *155*, 96−127.

(43) Kay, D.; Welford, R. Efficient Numerical Solution of Cahn-Hilliard-Navier-Stokes Fluids in 2D. *SIAM J. Sci. Comput.* **2007**, *29*, 2241−2257.

(44) Voigt, A.; Witkowski, T. A multi-mesh finite element method for Lagrange elements of arbitrary degree. *J. Comput. Sci.* **2012**, *3*, 420−428.

(45) AMDiS is freely available for research and teaching purposes and can be downloaded at url: http://www.simunova.com.

(46) Aland, S. Modelling of two-phase flow with surface active particles. Ph.D. Thesis, Technische Universität Dresden, 2012; url: http://nbn-resolving.de/urn:nbn:de:bsz:14-qucosa-92397.

(47) Nickerl, J.; Helbig, R.; Schulz, H. J.; Werner, C.; Neinhuis, C. Diversity and potential correlations to the function of Collembola cuticle structures. *Zoomorphology* **2012**, DOI: 10.1007/s00435-012-0181-0.

(48) Rasband, W. *Image J*; 1997−2012; url: http://imagej.nih.gov/ij/
.